PNAS RESEARCH ARTICLE | NEUROSCIENCE

Prestin's fast motor kinetics is essential for mammalian cochlear amplification

Satoe Takahashi[a], Yingjie Zhou[b], Takashi Kojima[a], Mary Ann Cheatham[b,c], and Kazuaki Homma[a,c,1]

Edited by Robert Fettiplace, University of Wisconsin-Madison, Madison, WI; received October 19, 2022; accepted February 6, 2023

Prestin (SLC26A5)-mediated voltage-driven elongations and contractions of sensory outer hair cells within the organ of Corti are essential for mammalian cochlear amplification. However, whether this electromotile activity directly contributes on a cycle-by-cycle basis is currently controversial. By restoring motor kinetics in a mouse model expressing a slowed prestin missense variant, this study provides experimental evidence acknowledging the importance of fast motor action to mammalian cochlear amplification. Our results also demonstrate that the point mutation in prestin disrupting anion transport in other proteins of the SLC26 family does not alter cochlear function, suggesting that the potential weak anion transport of prestin is not essential in the mammalian cochlea.

prestin | SLC26A5 | DFNB61 | electromotility | cochlear amplification

Prestin (SLC26A5) belongs to the solute carrier 26 (SLC26)/sulfate permease family and is abundantly expressed in the lateral membrane of the cochlear outer hair cells (OHCs) (1, 2). This membrane-based molecular motor is responsible for voltage-dependent somatic contraction and elongation of OHCs, referred to as electromotility (3). Its importance for mammalian cochlear amplification was demonstrated using prestin knockout (KO) mouse models that showed approximately 50 dB threshold elevations across frequency (4–7). However, these KO mouse models fell short of defining the role of prestin-mediated electromotility because deletion of prestin not only abolishes electromotility, but it also drastically reduces the length and axial stiffness of OHCs. Reduction of OHC stiffness per se likely affects cochlear amplification, as OHCs are part of the organ of Corti structure in which the basilar membrane, Deiters' cells, OHCs, and tectorial membrane operate within a tightly coupled feedback loop. A later study addressed this issue by generating a knockin (KI) mouse model expressing V499G/Y501H-prestin, which is virtually nonfunctional but targets the lateral membrane to confer normal OHC morphology and stiffness (8). The prestin-KO-like hearing phenotype found in this KI mouse model demonstrated that prestin-mediated electromotility is indeed essential for mammalian hearing. However, it still remains elusive whether prestin contributes to the mechanical amplification process on a cycle-by-cycle basis, given the controversy surrounding prestin's activation at high frequencies (9–18). Another outstanding question relates to the contribution of prestin to the survival of OHCs. It is conceivable that the weak anion transport function of prestin (19) may be essential for maintaining the ionic homeostasis within OHCs because prestin-KO mice suffer progressive OHC loss (4, 5). However, the physiological relevance of prestin's anion transport function remains undefined.

If prestin contributed to cochlear amplification on a cycle-by-cycle basis, an experimental manipulation that slows the motor kinetics of prestin should impair hearing. Likewise, if the anion transport function of prestin were essential for OHC maintenance, an experimental manipulation that specifically abolishes the anion transport function of prestin should induce OHC death. Using a genetic approach, this study shows that a KI mouse model expressing a deafness-associated prestin variant, R130S-prestin, with slowed motor kinetics, exhibits frequency-dependent reductions in sensitivity, which was restored by introducing an additional missense change, p.S396D (R130S/S396D-prestin) that mimics the chloride-bound state of the motor protein. Our study also shows that missense changes equivalent to p.S396D in mammalian prestin completely abrogate the anion transport function of SLC26 proteins, but that mice expressing S396D-prestin do not exhibit OHC dysfunction or death. These observations suggest that mammalian prestin is specialized for mechanical amplification on a cycle-by-cycle basis, and that its weak anion transport function is a vestige of molecular evolution with minimal physiological contribution to mammalian hearing.

Significance

Prestin is an essential motor protein for outer hair cell (OHC)-based cochlear amplification. However, it is not fully understood how prestin contributes to the mechanical sound amplification process. It is also not known if prestin's weak anion transport function makes any physiological contribution to OHC survival. In this study, we provide experimental evaluation of these outstanding questions using mouse models in which the motor kinetics of prestin was significantly slowed or the anion transport function of prestin was specifically abrogated without affecting the motor function. Our results support the contribution of prestin's fast motor kinetics in normal hearing and argue against the contribution of prestin's weak transport function for OHC maintenance.

Results

The p.R130S Prestin Missense Variant Induces Hearing Loss. The p.R130S (c.390A>C) missense variant was identified in the prestin gene, *SLC26A5*, of patients with bilateral

Author contributions: K.H. designed research; S.T., Y.Z., T.K., M.A.C., and K.H. performed research; S.T., Y.Z., T.K., M.A.C., and K.H. analyzed data; and S.T., M.A.C., and K.H. wrote the paper.

The authors declare no competing interest.

This article is a PNAS Direct Submission.

[1]To whom correspondence may be addressed. Email: k-homma@northwestern.edu.

This article contains supporting information online at https://www.pnas.org/lookup/suppl/doi:10.1073/pnas.2217891120/-/DCSupplemental.

Published March 9, 2023.

sensorineural hearing loss (20). Our previous study characterized this missense variant in a heterologous expression system and found that it slows the motor kinetics of prestin (21). To define the pathophysiological relevance of this finding, we generated a KI mouse model expressing R130S-prestin and measured auditory brainstem responses (ABRs) (Fig. 1*A*) and distortion product otoacoustic emissions (DPOAEs) (Fig. 1*B*). The ABR and DPOAE thresholds were elevated in R130S-prestin homozygous mice in a frequency-dependent manner, whereas heterozygotes were comparable to wild-type (WT) littermates, which is in line with the recessive nature of the p.R130S missense variant (20). Cytocochleograms (Fig. 2) found only minor OHC loss within the tested frequency range (8 to 32 kHz), suggesting that OHC dysfunction, not loss, accounts for the hearing phenotype in R130S-prestin homozygous mice. The frequency-dependence of the ABR and DPOAE threshold shifts (Fig. 1 *A* and *B*, *Right*) implies reduced mechanical activity of R130S-prestin with increasing frequency, consistent with our previous study showing slowed motor kinetics for this prestin variant (21).

The Biophysical Mechanism of the p.R130S Prestin Variant. Recently solved structures of SLC26A4 (pendrin) (22), SLC26A5 (prestin) (23–26), and SLC26A9 (27, 28) provide mechanistic insights into the anion transport and motor functions of the SLC26 proteins. Both the anion substrate binding site and translocation pathway located between the core and gate domains have been structurally defined (Fig. 3 and *SI Appendix*, Fig. S1). The remarkable resemblance among these SLC26 protein structures suggests a common molecular mechanism underlying the motor and anion transport functions of the SLC26 proteins. Arg^{130} in prestin is conserved among most SLC26 proteins except for SLC26A7, A8, and A9 (histidine instead of arginine). This arginine residue is not associated with the anion translocation pathway but is located close to the intracellular entrance of the anion translocation pore, contributing to the positively charged microenvironment (Fig. 3 and *SI Appendix*, Fig. S1).

Chloride is an extrinsic cofactor (29) essential for prestin's fast motor kinetics (30). Although the intracellular chloride concentration in mature OHCs is estimated to be 10 mM or less (31), it is conceivable that the positively charged microenvironment assures that the chloride concentration around the intracellular side of the anion translocation pathway is sufficient for fast electromotility. Based on this premise, introduction of a negative charge that mimics chloride binding at the anion binding site in R130S-prestin should restore fast motility and sensitivity. To explore this possibility, we generated additional KI mouse models expressing S396D-prestin and R130S/S396D-prestin in light of preceding studies showing that introduction of a negatively charged residue at the Ser^{396} site (p.S396D or p.S396E) made prestin insensitive to intracellular chloride and constitutively active (32, 33). We chose p.S396D over p.S396E because the electrophysiological properties of S396D-prestin were more WT-like compared with S396E-prestin (*SI Appendix*, Fig. S2). The recently solved cryogenic electron microscopy (cryo-EM) structures of prestin with bound chlorides confirm that p.S396D mimics a chloride-bound state (Fig. 4*A*). We found that both S396D-prestin and R130S/S396D-prestin homozygous mice show drastically improved ABR and DPOAE thresholds that were virtually WT-like (Fig. 4 *B* and *C*).

We also examined the electrophysiological properties of OHCs isolated from prestin KI mouse models using the whole-cell patch-clamp recording technique (Fig. 5*A*) to measure electromotility (Fig. 5*B*) and its concurrent electrical signature, nonlinear capacitance (NLC) (Fig. 5*C*). Although OHCs expressing R130S-prestin are electromotile, the magnitude is smaller when compared to WT. In contrast, S396D-prestin-expressing OHCs showed WT-like electromotility (Fig. 5*D*). Interestingly, the introduction of p.S396D, which restored sensitivity in R130S/S396D-prestin mice (Fig. 4 *B* and *C*), did not restore WT-like electromotility in R130S/S396D-prestin (Fig. 5*D*). Statistically significant differences in α (voltage sensitivity), V_{pk} (voltage operating point),

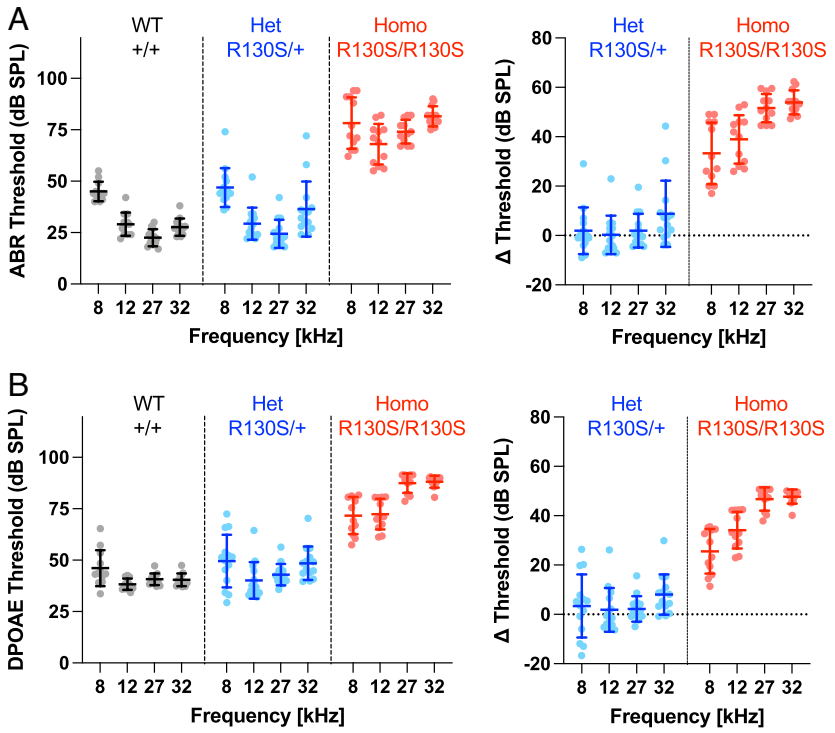

Fig. 1. ABRs and DPOAEs in R130S-prestin KI mice. ABR (*A*) and DPOAE (*B*) thresholds for WT littermate controls ($Slc26a5^{+/+}$) heterozygotes ($Slc26a5^{R130S/+}$), and homozygotes ($Slc26a5^{R130S/R130S}$) determined at P31–37. *Right* panels show differences in thresholds with respect to the WT controls. Horizontal solid lines indicate means and SDs (*Left*), or propagated errors (*Right*) calculated from SDs of the original data shown in *Left* panels.

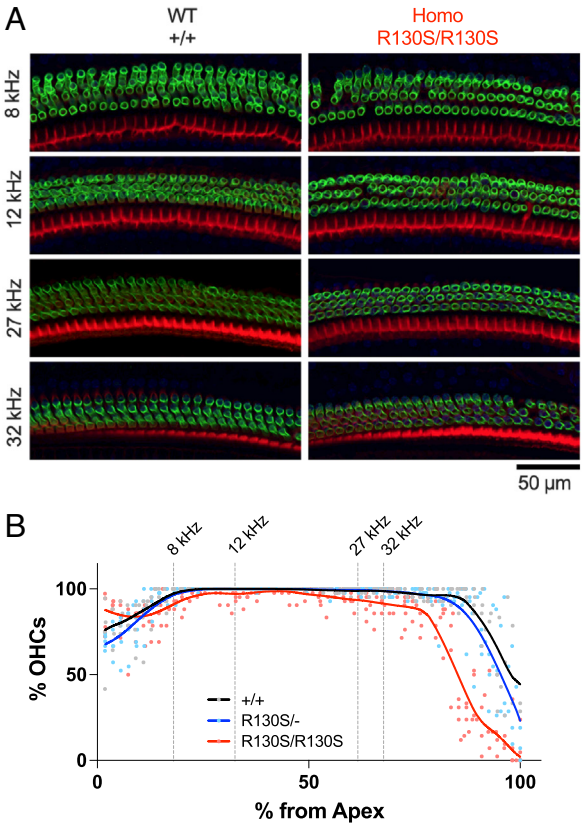

Fig. 2. OHC cytocochleograms of R130S-prestin KI mice. (*A*) Fluorescent images of P42 organ of Corti whole-mount samples from *Slc26a5*$^{+/+}$ and *Slc26a5*$^{R130S/R130S}$ mice, stained with anti-prestin antibody (green) and phalloidin-Alexa568 (red). (*B*) Cytocochleograms for *Slc26a5*$^{+/+}$ (n = 4), *Slc26a5*$^{R130S/+}$ (n = 5), and *Slc26a5*$^{R130S/R130S}$ (n = 5) (P42 for all). Solid lines indicate Locally Weighted Scatterplot Smoothing (LOWESS) fits. Cochlear locations corresponding to the frequencies tested for the ABR and DPOAE measurements (Fig. 1) are indicated by vertical broken lines.

C_{lin} (proportional to the cell size), and NLC_{pk} (the peak magnitude of NLC) between WT vs. R130S-prestin (Fig. 5*E*) were observed when quantifying the NLC parameters. Since the magnitude of the C_{lin} value reflects the amount of the prestin protein targeted to the lateral membrane of OHCs (4, 7, 34), the reduction in C_{lin} implies reduced membrane targeting of R130S-prestin, which is consistent with partially impaired membrane targeting of R130S-prestin in HEK293T cells (21). It is emphasized that these changes in motor properties are not likely to account for the hearing deficits found in R130S-prestin homozygous mice (Fig. 1), because the introduction of p.S396D did not restore WT-like electromotility and NLC_{pk} in R130S/S396D-prestin (P = 0.56 and 0.07 (R130S-prestin vs. R130S/S396D-prestin), respectively, Fig. 5 *D* and *E*) even though restoration of peripheral sensitivity was achieved in R130S/S396D-prestin mice (Fig. 4). This result may not seem intuitive, but it is consistent with reports showing that mammalian cochlear function is minimally affected by large reductions in prestin protein (34, 35).

To further explore the biophysical mechanism of the p.R130S prestin variant, we also measured NLC as a function of stimulus frequency and intracellular chloride in OHCs expressing WT-prestin, S396D-prestin, R130S-prestin, and R130S/S396D-prestin (Fig. 6). We found that the motor kinetics of WT-prestin is slower at 1 mM chloride compared with that measured at 144 mM intracellular chloride (Fig. 6*A*), consistent with a previous study (30). As anticipated, the motor kinetics of S396D-prestin were fast and insensitive to low chloride (1 mM) (Fig. 6*A*), confirming that p.S396D mimics chloride binding and supports fast electromotility independent of chloride concentration. In contrast, reduction in motor kinetics for R130S-prestin at 1 mM chloride was much greater compared with WT-prestin, whereas the motor kinetics of R130S/S396D-prestin measured at 1 mM chloride was faster than R130S-prestin measured at 144 mM chloride (Fig. 6*B*). These observations support the idea that positively charged Arg^{130} augments chloride binding affinity, thereby supporting fast electromotility. The recovery of hearing sensitivity in the double mutant shows the importance of prestin's fast electromotility for cochlear amplification.

It is interesting to note that expression of the sodium-potassium-chloride cotransporter *Slc12a2* (NKCC1) declines postnatally, while the potassium-chloride cotransporter *Slc12a7* (KCC4) increases gradually (36, 37) [browsable using the gEAR portal (38)]. These results imply that the chloride concentrations in young postnatal OHCs may be higher than in adult OHCs. The dynamics of these expression patterns may help to explain why young R130S-prestin homozygous mice (P19-P22) had lower DPOAE thresholds at 8 and 12 kHz when compared with older animals (*SI Appendix*, Fig. S3). This observation cannot be due to a larger prestin expression in young OHCs, because the magnitudes of NLC and

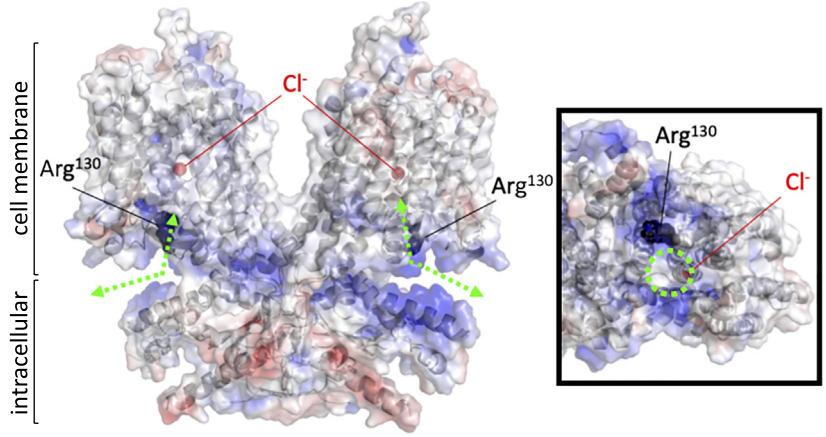

Fig. 3. An electrostatic potential map of the prestin protein. A ribbon representation of homodimeric human prestin (PDB ID: 7LGU) with surface electrostatic potentials calculated by PyMOL (blue and red indicate positive and negative changes, respectively). The Arg^{130} residues (black) and bound chlorides (red) are indicated by spheres. Green dashed lines with double arrows indicate presumed anion translocation paths. An intracellular view of one of the protomers is shown in a box on the right. A dashed green circle indicates the intracellular entrance to the anion binding site.

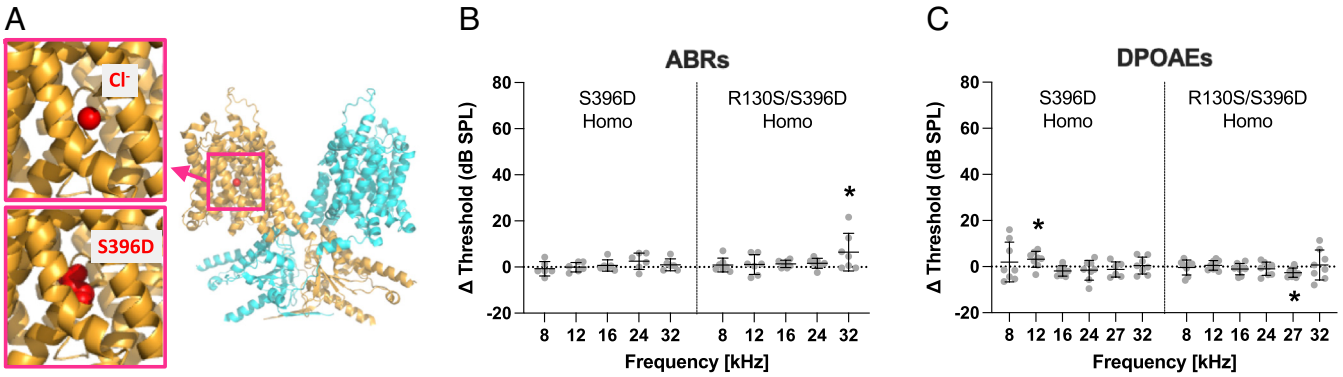

Fig. 4. Effects of p.S396D on ABR and DPOAE thresholds. (*A*) A bound chloride and p.S396D (modeled by PyMOL) within the human prestin structure (PDB ID: 7LGU) are indicated by red spheres. ABR (*B*) and DPOAE (*C*) threshold shifts (compared to WT) for S396D-prestin and R130S/S396D-prestin homozygous mice determined between P29 and 43. Short horizontal solid lines indicate means and propagated errors calculated from SDs of the threshold data. A dashed horizontal line at 0 dB SPL is provided for reference and signifies no change in sensitivity between mutant and control. "*", $0.01 \le P < 0.05$.

electromotility were found to be comparable to measurements in OHCs at 1- to 1.5-mo of age (*SI Appendix*, Fig. S4). Hence, these observations further support the proposed pathological mechanism of R130S-prestin being ascribed primarily to its reduced chloride binding and associated slower motor kinetics in more mature OHCs. It is also noted that the large, age-independent threshold shifts seen in R130S-prestin homozygotes at 27 and 32 kHz (*SI Appendix*, Fig. S3) may relate to the inability of R130S-prestin to attain maximal motor kinetics even at 144 mM chloride (Fig. 6*B*) (21).

The Anion Transport Function of Prestin Does Not Contribute to OHC Maintenance. A previous study reported a weak $2HCO_3^-/Cl^-$ electrogenic antiport activity for mammalian prestin, implying a role in maintaining ion homeostasis in OHCs (19). Using OHCs isolated from WT mice, we evaluated $2HCO_3^-/Cl^-$ antiport activity in the whole-cell configuration. The bath solution contained 148 mM chloride, while the intracellular solution contained 10 mM chloride with or without 10 mM $NaHCO_3$. Cobalt and cesium ions were included in both solutions to minimize the cation conductance (*Materials and Methods*). The Nernst equilibrium potentials calculated for chloride (E_{Cl}) and bicarbonate (E_{HCO3}) are –69 mV and +106 mV (with 10 mM intracellular $NaHCO_3$), respectively. Since the reversal potential (V_{rev}) for $2HCO_3^-/Cl^-$ electrogenic antiport is computed as $2E_{HCO3}–E_{Cl}$, we anticipated finding a positive V_{rev} for the intracellular solution containing 10 mM $NaHCO_3$. However, V_{rev} values measured with intracellular $NaHCO_3$ (–4.0 ± 4.5 mV, mean ± SD, n = 12) were small and

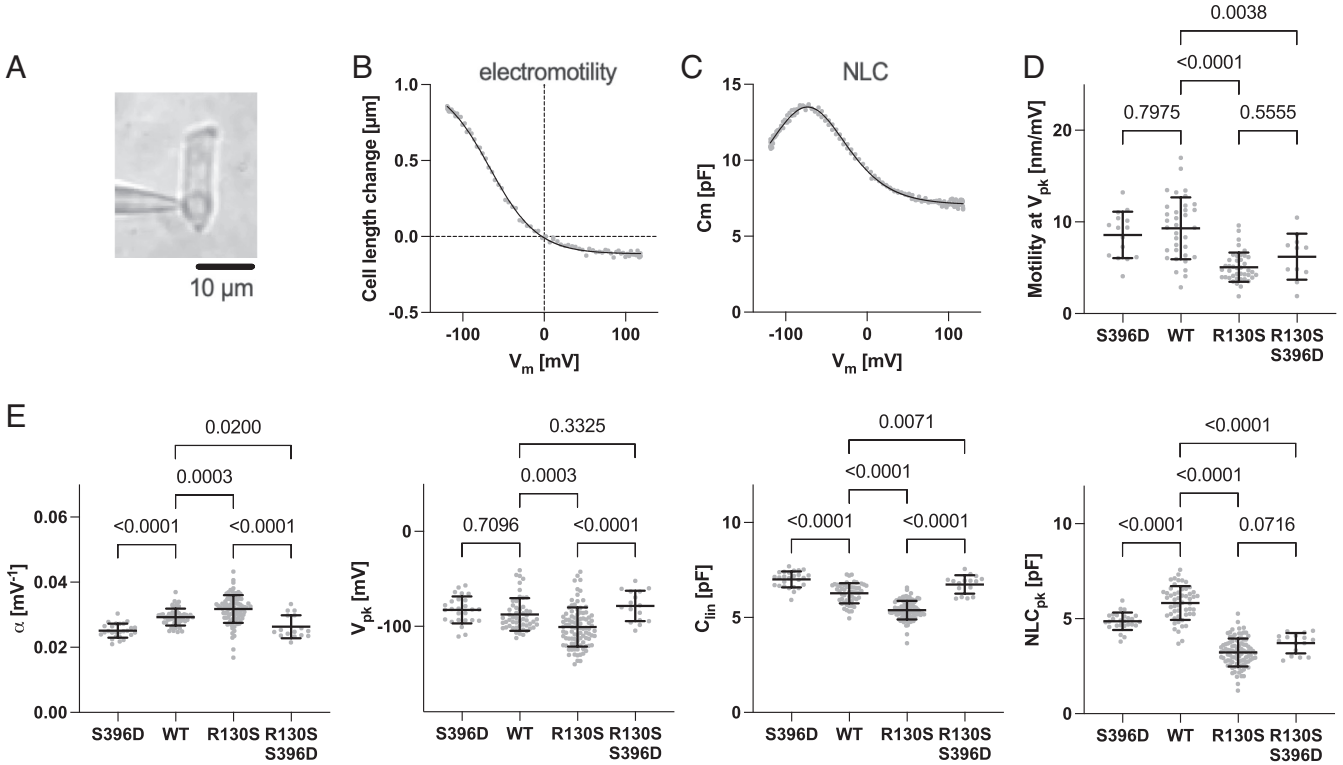

Fig. 5. Electromotility and NLC recordings in OHCs. (*A*) Whole-cell recording configuration established in an isolated OHC (WT). Examples of electromotility (*B*) and NLC (*C*) measurements (WT). Solid lines indicate two-state Boltzmann curve fits. Summaries of electromotility (*D*) and NLC parameters (*E*) recorded in OHCs isolated from R130S-prestin, S396D-prestin, and R130S/S396D-prestin homozygous mice and WT controls. NLC_{pk}, the magnitude of NLC at V_{pk}. The *P* values were computed by one-way ANOVA followed by Tukey's multiple comparison procedure. Horizontal solid lines indicate the means and SDs. OHCs were collected from the apical region (corresponding to 4 to 10 kHz) of the cochlea and obtained from mice between P30 and 53.

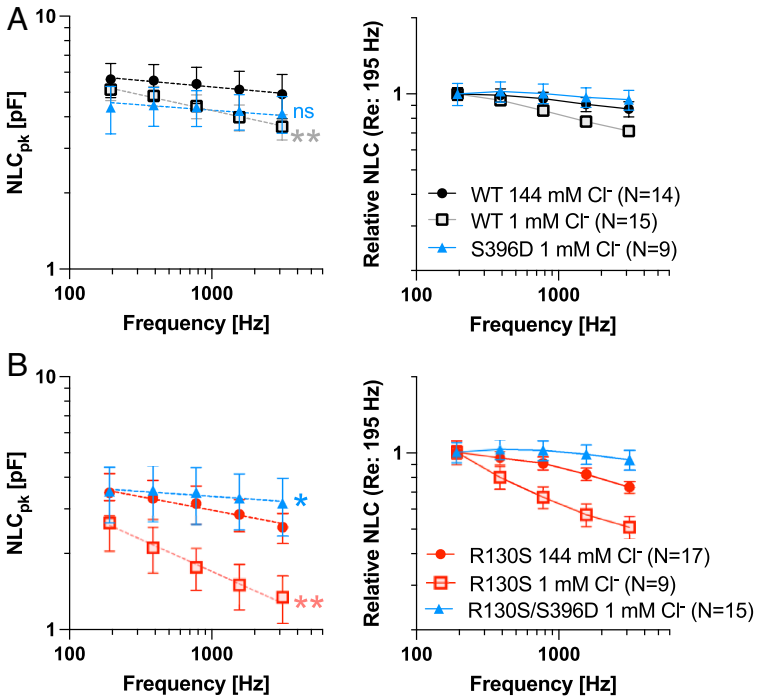

Fig. 6. The effect of p.S396D on the motor kinetics of prestin. Stimulus frequency-dependent NLC was measured in OHCs isolated from WT (*A*), S396D-prestin (*A*), R130S-prestin (*B*), and R130S/S396D-prestin (*B*) homozygous mice under high (144 mM) and low (1 mM) intracellular chloride conditions using five different f_1 frequencies (195, 390, 781, 1,563, and 3,125 Hz) with the corresponding f_2 frequencies being twice as large as f_1 (i.e., 390, 780, 1,563, 3,125, 6,250 Hz). Dashed lines through data points in *Left* panels indicate the double-log linear regression from which *P* values (compared with "WT 144 mM Cl^-" in *A* or "R130S 144 mM Cl^-" in *B*) were determined by *F*-tests. "ns", not significant ($P \geq 0.05$); "*", $0.01 \leq P < 0.05$; "**", $0.001 \leq P < 0.01$. Relative NLC shown in *Right* panels allow for a clearer appreciation of differences in frequency responses (motor kinetics). Error bars in *Left* panels indicate SDs, while those in *Right* panels indicate propagated errors calculated from SEs of the original data shown in *Left* panels. OHCs were collected from mice at P27-63.

were statistically insignificant when compared with V_{rev} without $NaHCO_3$ (−5.5 ± 6.0 mV, mean ± SD, n = 12) ($P > 0.05$) (*SI Appendix*, Fig. S5 *A* and *B*). Whole-cell currents measured at a 0 mV holding potential in the presence and absence of intracellularly added $NaHCO_3$ were also small and statistically indistinguishable ($P > 0.05$) (*SI Appendix*, Fig. S5*C*), suggesting that prestin-mediated $2HCO_3^-/Cl^-$ antiport activity is minimal.

The S396D-prestin KI provides a fortuitous opportunity to examine the physiological relevance of the anion transport function of mammalian prestin. Given that Ser^{396} is located at the anion substrate binding site (23–26), introduction of a negatively charged residue at Ser^{396} in mammalian prestin or at equivalent sites in nonmammalian prestin orthologs or other SLC26 family proteins should abrogate anion transport function. Since the anion transport activity of mammalian prestin is too small to be detected in our hands (see above), we introduced equivalent missense changes to Ser^{402} and Ser^{399} in nonmammalian prestin orthologs, chicken (cPres) and zebrafish prestin (zPres), respectively. The electrogenic SO_4^{2-}/Cl^- antiport activity reported for these nonmammalian prestin orthologs (39) allowed electrophysiological assessments of their transport activities. Specifically, we measured net inward current (efflux of SO_4^{2-} and influx of Cl^-) induced by an outward SO_4^{2-} gradient combined with an inward Cl^- gradient (*Materials and Methods*) in HEK293T cells at a 0 mV holding potential. Consistent with a previous report (39), significant inward currents were detected in cells expressing WT-cPres and WT-zPres (Fig. 7*A*). In contrast, currents measured in cells expressing S402D-cPres, S402E-cPres, S399D-zPres, and S399E-zPres were indistinguishable from noninduced negative controls (Fig. 7*A*), affirming that these negatively charged residues disable prestin's anion transport.

To explore the generality of these findings, we turned to SLC26A4 and SLC26A9 whose recently solved structures (22, 27, 28) allow visual confirmation of the locations of residues equivalent to Ser^{396} in prestin (SLC26A5), i.e., Ala^{406} and Ala^{390} in SLC26A4 and SLC26A9, respectively. The electroneutral monovalent anion antiport mode of SLC26A4 does not allow electrophysiological determination of its transport activity. Therefore, we fluorometrically determined HCO_3^-/Cl^- (Fig. 7 *B*, *Left*) and I^-/Cl^- (Fig. 7 *B*, *Right*) antiport activities in HEK293T cells heterologously expressing human SLC26A4 (WT-hA4), A406D-hA4, or A406E- hA4 in a doxycycline-dependent manner. Consistent with a previous report (40), WT-hA4 showed doxycycline dosage-dependent increases in HCO_3^-/Cl^- and I^-/Cl^- antiport activities, whereas A406D-hA4 and A406E-hA4 showed very small doxycycline-independent transport activities that were indistinguishable from those of negative controls (shaded regions) (Fig. 7*B*). We also performed this fluorometric HCO_3^-/Cl^- antiport assay for HEK293T cells expressing mouse prestin (WT). However, we could not detect prestin-mediated HCO_3^-/Cl^- antiport activity despite the ability of the assay to detect very small residual transport activities of disease-associated hA4 variants (40). Because of the channel-like fast anion transport activity of SLC26A9 (41, 42), a straightforward electrophysiological determination of its anion transport can be obtained by simply measuring transmembrane chloride conductance (Fig. 7 *C*, *Left*). The whole-cell conductance of HEK293T cells expressing WT human SLC26A9 (WT-hA9) was very large and limited by the series resistance in some recordings, which resulted in an underestimation of the mean value of the anion transport activity of WT-hA9 (indicated by an upward arrow in Fig. 7 *C*, *Left*). In contrast, the whole-cell conductance measured in cells expressing A390D-hA9 and A390E-hA9 was similar to that of noninduced negative controls (Fig. 7 *C*, *Left*). We also performed the fluorometric I^- transport assay for A390D-hA9 and confirmed the absence of transport activity in A390D-hA9 (Fig. 7 *C*, *Right*).

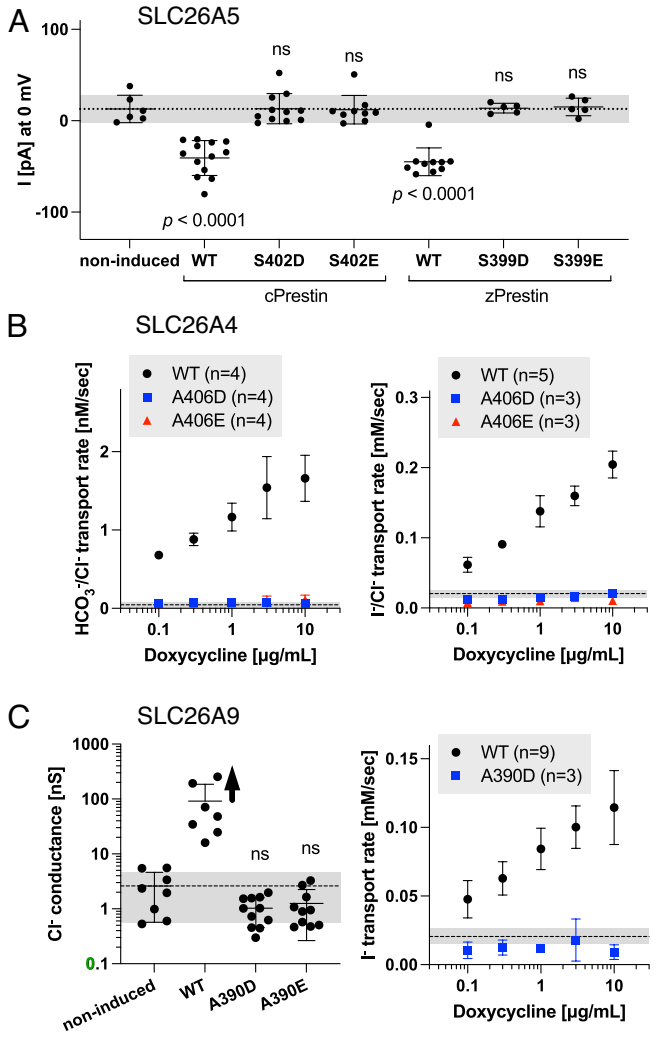

Fig. 7. Anion transport assays for the SLC26 proteins. (*A*) Electrophysiological SO_4^{2-}/Cl^- antiport assays in stable HEK293T cell lines heterologously expressing chicken (cPrestin) and zebrafish (zPrestin) constructs in a doxycycline-inducible manner (1 µg/mL one day prior to experiment). (*B*) Fluorometric HCO_3^-/Cl^- (*Left*) and I^-/Cl^- (*Right*) antiport assays in stable HEK293T cell lines heterologously expressing human pendrin constructs in a doxycycline-inducible manner (0.1 to 10 µg/mL 1 d prior to experiment). (*C*) Electrophysiological chloride transport (*Left*) and fluorometric iodide transport (*Right*) assays in stable HEK293T cell lines heterologously expressing human SLC26A9 constructs in a doxycycline-inducible manner (1 µg/mL 1 d prior to experiment). In all panels, the short horizontal solid lines indicate the means and SDs, while the horizontal broken line with gray shading indicates the basal transport activity (means ± SDs) of noninduced cells (negative controls).

Collectively, these observations point to complete abrogation of the anion transport by the p.S396D missense change in mammalian prestin. To confirm, we also performed the electrophysiological transport assay in OHCs isolated from S396D-prestin homozygous mice but could not detect HCO_3^-/Cl^- antiport activity, similar to observations made in WT controls (see above): The V_{rev} value of S396D-prestin-expressing OHCs with an intracellular solution containing 10 mM bicarbonate (−8.8 ± 5.3 mV, mean ± SD, n = 3) was negative and statistically indistinguishable (P > 0.05) from WT controls (in the presence of 10 mM bicarbonate, −4.0 ± 4.5 mV, mean ± SD, n = 12; in its absence, −5.5 ± 6.0 mV, mean ± SD, n = 12). These results confirm the absence of detectable transport activity in S396D-prestin-expressing OHCs. Nevertheless, S396D-prestin homozygous mice show WT-like ABR and DPOAE thresholds (Fig. 4) and their OHC cytocochleograms are similar to WT even at ~7 mo of age (Fig. 8). These results suggest that the reportedly weak anion transport activity of mammalian prestin is of minimal physiological importance for OHC function and maintenance. Our study strongly suggests that prestin evolved to mechanically amplify sound-induced displacements of the organ of Corti on a cycle-by-cycle basis in the mammalian cochlea, and that its very weak anion transport is the vestigial remnant from an ancestral anion transporter.

Discussion

Tonotopically graded changes in the length and conductance of OHCs (shorter and greater toward the base) (43) imply an evolutionary pressure to reduce the resistance-capacitance membrane time constant to drive prestin-based fast electromotility. However, it remains contentious whether prestin can produce sufficient mechanical output at high frequencies. It is conceivable that prestin may not be the sole molecular player contributing to high-frequency signal coding (44, 45). In any case, if prestin mechanically contributes to cochlear amplification on a cycle-by-cycle basis, a prestin mutation that slows motor kinetics should impair hearing, at least partially. Our previous study found that the p.R130S missense variant slows the motor kinetics of prestin (21). Encouraged by this finding, we generated the R130S-prestin KI mouse model in this study and found that homozygous mutants show frequency-dependent threshold shifts, i.e., greater shifts at high frequencies (Fig. 1). We also found that adding a second mutation, p.S396D, confers chloride-independent fast motor kinetics (Fig. 6) and restores hearing sensitivity (Fig. 4). Moreover, we found that S396D-prestin does not affect OHC function (Fig. 4) or maintenance (Fig. 8) despite complete abrogation of anion transport demonstrated in nonmammalian prestin orthologs and other SLC26 family proteins (Fig. 7). Taken together, the observations reported here point to a dedicated role of prestin as a mechanical cochlear amplifier working on a cycle-by-cycle basis in mammalian ears, although a question still remains regarding how much prestin's motor activity can be elicited at high frequencies as our measurements of prestin kinetics are limited to relatively low frequencies (Fig. 6).

A previous study reported four prestin splicing isoforms with the longest (full-length) predominating (46). In light of the recently solved prestin structures (23–26) and functional data (47), it is probable that none of the three short isoforms is functional. In other words, only one type of functional prestin protein is likely expressed in OHCs regardless of cochlear location. Thus, it is legitimate to assume that the motor kinetics of middle and basal OHCs is similar to that determined in this study for apical OHCs with

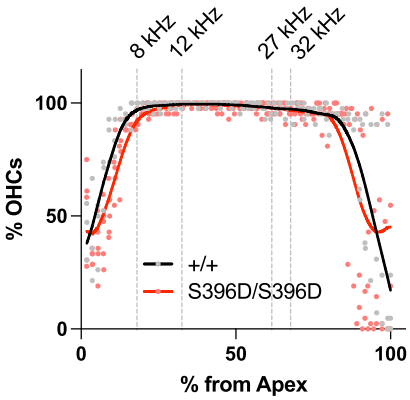

Fig. 8. OHC cytocochleograms in S396D-prestin homozygous mice. Average OHC loss is plotted along the cochlear spiral from apex to base for WT controls (n = 3) and S396D-prestin homozygous (n = 5) mice at approximately 7 mo of age (P196-219). Solid lines indicate LOWESS smoothing fits.

characteristic frequencies between 4 and 10 kHz (Fig. 6). It is possible that the motor kinetics of prestin may be modulated by the density of the prestin protein in the lateral membrane of OHCs. The presence of an apical-basal gradient in prestin density was claimed by two functional studies (48, 49) but opposed by an anatomical study (50). In any case, it seems unlikely that the difference in the motor kinetics between WT-prestin and R130S-prestin becomes smaller or comparable at high frequencies.

Chloride is known to support prestin's fast motor kinetics (30). Subsequent identification of a bound chloride in cryo-EM structures (23, 26) defined the anion binding site within the prestin protein and explicitly explained why p.S396D mimics the chloride-bound state (Fig. 4*A*). Slowed motor kinetics of R130S-prestin and its restoration by p.S396D suggest an indirect contribution of the positively charged Arg^{130} to fast electromotility by augmenting chloride binding under the low-chloride condition in mature OHCs. The prestin structures solved under various anion substrate conditions suggest that voltage-induced relative motions of the gate domains with respect to the core domains (i.e., the transition between "inward-open" and "occluded" states) account for the molecular mechanism underlying electromotility (23, 24, 26). The anion binding site is located at the interface of the gate and core domains and is positively charged due to Arg^{399} and the N-terminal positive dipoles of the TM3 and TM10 helices pointing toward the anion binding site. This charged environment likely poses a significant energy barrier between contracted and expanded states, which may slow state transition kinetics. In addition, a gate/core interdomain hydrogen bonding network can be formed between Gln^{97} and Asn^{447} (26), which would also contribute to the energy barrier. Chloride binding neutralizes the positively charged environment and likely modulates the interdomain hydrogen bonding interaction (26), which would collaboratively lower the energy barrier and allow fast state transitions, i.e., fast electromotility.

Although prestin is essential for normal hearing, cochlear function can tolerate large reductions in prestin activity (34, 35). This is counterintuitive considering prestin's cycle-by-cycle action is presumed to be significantly attenuated at high frequencies. It is, therefore, conceivable that electromotility may be supported by OHC turgor pressure, allowing prestin to generate force indirectly by modulating the axial stiffness of the cell in a voltage-dependent manner (35, 51, 52). Such a model can explain why cochlear function tolerates large reductions in prestin expression but not in motor kinetics.

Materials and Methods

Animals. Prestin mouse models harboring p.R130S, p.S396D, or both p.R130S/p.S396D were generated on the FVB/NJ background using CRISPR/Cas9 at Northwestern University's Transgenic and Targeted Mutagenesis Laboratory. Founders were crossed with WT FVB/NJ mice for at least two generations, and the resulting N2 offspring screened for the top five off-target loci. Established mouse lines were maintained in-house by heterozygous mating and genotyped by Transnetyx (Cordova, TN). All procedures and protocols were approved by Northwestern University's Institutional Animal Care and Use Committee and by National Institute on Deafness and Other Communication Disorders (NIDCD).

Generation of Stable Cell Lines. Plasmids encoding chicken (cPres) and zebrafish prestin (zPres) were kindly provided by Dominik Oliver (Philipps University, Marburg), and a plasmid containing human SLC26A9 (hA9) complementary DNA was a gift from Dr. Tomohiro Shima (University of Tokyo, Tokyo). These constructs were cloned into a pSBtet-pur vector (Addgene) using SfiI sites with a C-terminal mTurquoise (mTq2) tag. C-terminally mTq2-tagged human SLC26A4 (hA4) cloned in a pSBtet-pur vector was previously generated in our laboratory (40). Mutagenic primers were used to introduce missense changes in these constructs (p.S402D/E for cPres; p.S399D/E for zPres; p.A406D/E for hA4; and A390D/E for hA9). Stable cell lines that express these SLC26 constructs in a doxycycline-dependent manner were established in HEK293T cells as previously described (40). Briefly, pSB plasmids were introduced together with pCMV(CAT)T7-SB100 (Addgene) using Effectene (Qiagen), and the transfected cells were selected in DMEM supplemented with 10% FBS and 1 μg/mL puromycin (Fisher Scientific).The hA4 and hA9 constructs were also introduced to the HEK293T-$mVenus^{H148Q/I152L}$ cell line that was generated in a previous study (40).

Hearing Tests. Anesthetized (100 mg/Kg ketamine/10 mg/Kg xylazine IP) animals were screened at various ages to determine the hearing phenotype using noninvasive methods. Both male and female mice were tested, and all recordings were from the animal's left ear in a sound-isolated and electrically shielded chamber. A heating pad was used to maintain body temperature at approximately 37 °C. Distortion product otoacoustic emissions (DPOAEs) were recorded using a custom probe placed close to the eardrum as described previously (53). DPOAE input–output functions (f_2/f_1 = 1.2) were collected at various f_2 frequencies, where $L_1 = L_2 + 10$ dB SPL, and used to determine DPOAE thresholds defined as the level of f_1 that produced a $2f_1$-f_2 component of 0 dB SPL. In contrast to otoacoustic emissions that reflect OHC function (54), auditory brainstem responses (ABR) reflect the integrity of the auditory nerve and brainstem pathways. These evoked potentials were recorded using three stainless steel needle electrodes inserted at the vertex, the mastoid and at the contralateral ear. The latter served as the common ground electrode, while the active vertex electrode was the noninverting (positive) and the reference mastoid electrode was the inverting (negative) electrode. ABRs were elicited using 5-ms tone bursts including the 0.5-ms rise/fall times and presented with a repetition rate of 20/s. Responses were amplified and filtered (300 to 2,000 Hz). Thresholds were obtained at various frequencies (8 to 32 kHz) by noting the stimulus level at which the waveform disappeared into the noise floor. Data are provided as threshold differences between mutants and controls.

NLC and Electromotility Measurements. OHCs were isolated as described previously (55). Whole-cell recordings were performed at room temperature using the Axopatch 200B amplifier (Molecular Devices) with a 10-kHz low-pass filter. Recording pipettes pulled from borosilicate glass were filled with either a high-chloride solution containing (mM) 140 CsCl, 2 $MgCl_2$, 10 EGTA, and 10 HEPES (pH 7.4) or a low-chloride solution containing (mM) 139 Cs-L-aspartate, 1 CsCl, 2 $MgSO_4$, 10 EGTA, and 10 HEPES (pH 7.4). Cells were bathed in an extracellular solution containing (mM) 120 NaCl, 20 TEA-Cl, 2 $CoCl_2$, 2 $MgCl_2$, 10 HEPES (pH 7.4). Osmolality was adjusted to 309 mOsmol/kg with glucose. Recordings were performed approximately 1 min after establishing the whole-cell configuration to ensure intracellular dialysis with the pipette solution. While recording, the intracellular pressure was not adjusted. The electric current response to a sinusoidal voltage stimulus (2.5 Hz, 120 or 150 mV amplitude) superimposed with two higher frequency stimuli (390.6 and 781.2 Hz, 10 mV amplitude) was recorded by jClamp (SciSoft Company). For stimulus frequency-dependent C_m measurements, f_1 was set at 195.3 (f_2 = 390.6), 390.6 (f_2= 781.3), 781.3 (f_2= 1,562.5), 1,562.5 (f_2= 3,125.0), and 3,125.0 (f_2= 6,250.0) Hz (21, 55) and a fast Fourier transform-based admittance analysis was used to determine C_m (56). Since both f_1 and f_2 contribute to C_m measurement, f_1 frequencies were used to report frequency-dependent NLC data (Fig. 6). OHC electromotility was captured using a Prosilica GE680 camera (Allied Vision) and the recorded sequential images analyzed using ImageJ as described previously (57).

NLC and Electromotility Data Analysis. Voltage-dependent C_m data were analyzed using the following two-state Boltzmann equation:

$$C_m = \frac{\alpha Q_{max} exp[\alpha(V_m - V_{pk})]}{\{1 + exp[\alpha(V_m - V_{pk})]\}^2} + C_{lin},$$

where a is the slope factor of the voltage-dependence of charge transfer, Q_{max} is the maximum charge transfer, V_m is the membrane potential, V_{pk} is the voltage at which the maximum charge movement is attained, and C_{lin} is the linear capacitance. Electromotility data were analyzed using the following equation:

$$D = \frac{D_{max}}{1 + exp[-\alpha(V_m - V_{pk})]} + D_0,$$

where D_{max} is the maximum cell length change, and D_0 is a base reference point at which an OHC shows zero cell contraction (at infinitely hyperpolarized membrane potential).

Electrophysiological Anion Transport Assay. To measure electrogenic $2HCO_3^-/Cl^-$ antiport in OHCs, recording pipettes pulled from borosilicate glass were filled with either a bicarbonate solution containing (mM) 124 Cs-L-aspartate, 6 CsCl, 10 $NaHCO_3$, 2 $MgCl_2$, 10 EGTA, and 10 HEPES (pH 7.4) equilibrated with 5% carbon dioxide or a minimal bicarbonate solution containing (mM) 134 Cs-L-aspartate, 6 CsCl, 2 MgCl, 10 EGTA, and 10 HEPES (pH 7.4) equilibrated with the atmospheric carbon dioxide (~400 ppm). The concentration of bicarbonate was indirectly determined by measuring pH. pH measured after 5% carbon dioxide bubbling (performed before every experiment) was typically ~7.3, indicating that the actual bicarbonate concentration in the 10 mM $NaHCO_3$-containing intracellular solution was ~9.7 mM (*SI Appendix*, Fig. S6). Isolated OHCs were bathed in a high-chloride solution containing (mM) 120 NaCl, 20 TEA-Cl, 2 $CoCl_2$, 2 $MgCl_2$, and 10 HEPES (pH 7.4). For measuring electrogenic SO_4^{2-}/Cl^- antiport in HEK293T cells expressing cPres or zPres constructs, recording pipettes were filled with a solution containing (mM) 10 CsCl, 10 Na_2SO_4, 130 potassium L-aspartate, 2 $MgCl_2$, 10 EGTA, and 10 HEPES (pH 7.4). Cells were bathed in a solution containing (mM) 120 NaCl, 20 TEA-Cl, 2 $CoCl_2$, 2 $MgCl_2$, and 10 HEPES (pH 7.4). For measuring Cl^- transport in HEK293T cells expressing hA9 constructs, recording pipettes were filled with a solution containing (mM) 140 CsCl, 2 $MgCl_2$, 10 EGTA, and 10 HEPES (pH 7.4). Cells were bathed in a solution containing (mM) 120 NaCl, 20 TEA-Cl, 2 $CoCl_2$, 2 $MgCl_2$, and 10 HEPES (pH 7.4). Command voltages were step functions of 30 ms duration (from −100 mV to +100 mV or −50 mV to +50 mV, in 10 mV steps). Holding potentials were set to 0 mV.

Fluorometric Anion Transport Assay. Doxycycline-inducible stable cell line-based HCO_3^-/Cl^- and I^-/Cl^- antiport assays were established and described in detail in a previous study (40). Briefly, stable HEK293T cells expressing C-terminally mTq2-tagged SLC26 protein constructs (for HCO_3^-/Cl^- antiport assay) or those with coexpressed iodide-sensitive fluorescent protein, $mVenus^{H148Q/I152L}$ (for I^-/Cl^- antiport assay), were cultured in a 12-well plate for 1 d following doxycycline application and dissociated with cell dissociation buffer (13150016, Thermo Fisher Scientific). For the HCO_3^-/Cl^- antiport assay, cells were loaded with a pH indicator, SNARF-5F (S23923, Thermo Fisher Scientific) in a high-chloride buffer containing (mM) 140 NaCl, 4.5 KCl, 1 $MgCl_2$, 2.5 $CaCl_2$, and 20 HEPES (pH 7.4) for 30 min in the presence of 5% CO_2 at room temperature. After removing unloaded SNARF dye, portions of the cell suspensions were transferred to wells in a 96-well plate (~1.5×10^5/well), and HCO_3^-/Cl^- the antiport assay initiated by an automated injection of a low-chloride buffer containing (mM) 125 Na-gluconate, 5 K-gluconate, 1 $MgCl_2$, 1 $CaCl_2$, 20 HEPES, and 25 $NaHCO_3$ with 5% CO_2 in Synergy Neo2 (Agilent/BioTek). For the I^-/Cl^- antiport assay, cells were resuspended in a high-chloride buffer containing (mM) 150 NaCl, 1 $MgCl_2$, 1 $CaCl_2$, and 20 HEPES (pH 7.5) for 30 min at room temperature and transferred to wells in a 96-well plate (~1.5×10^5/well). The I^-/Cl^- antiport assay was initiated by an automated injection of a high-iodide buffer containing (mM) 150 NaI, 1 $MgCl_2$, 1 $CaCl_2$, and 20 HEPES (pH 7.5). The fluorescence of SNARF-5F (for HCO_3^-/Cl^- antiport assay) or $mVenus^{H148Q/I152L}$ and mTq2 (for I^-/Cl^- antiport assay) was measured in a time-dependent manner using the Synergy Neo2 plate reader (Agilent/BioTek) and the data analyzed offline as described previously (40).

Cytocochleograms. Mice were cardiac perfused with 4% paraformaldehyde and cochleae extracted. After postfixation and decalcification, cochleae were dissected following the Eaton-Peabody Laboratory cochlear dissection protocol for whole mounts (58). Cochleae were stained with anti-prestin (59) followed by goat anti-rabbit Alexa Fluor 488 secondary antibody (ThermoFisher), together with Alexa Fluor 568 phalloidin and Hoechst 33342 (ThermoFisher) for actin and nuclei, respectively. Images were taken using a Leica DM IRB fluorescence microscope and a Nikon A1R confocal microscope for OHC counts as previously described (60). Cochlear locations corresponding to the frequencies tested for the ABR and DPOAE measurements (Fig. 1) were determined based on the Müeller et al. frequency place map (61). LOWESS smooth fits (62) were included in summary figures to facilitate visual inspection of the results.

Calculations of Propagated Errors. The uncertainties (σ) associated with subtraction and division computations to determine the differences in hearing thresholds with respect to the wild-type controls (Figs. 1 and 4 and *SI Appendix*, Fig. S3) and relative magnitudes of NLC measured at different stimulus frequencies with respect to those measured at 195 Hz (f_2 = 391 Hz) (Fig. 6) were calculated by the following equations:

$$\sigma_{A-B} = \sqrt{\sigma_A^2 + \sigma_B^2} \qquad \text{(for subtraction computations)},$$

$$\sigma_{A/B} = \left|\frac{A}{B}\right| \sqrt{\left(\frac{\sigma_A}{A}\right)^2 + \left(\frac{\sigma_B}{B}\right)^2} \qquad \text{(for division computations)},$$

where A and B are the mean values with associated errors, σ_A and σ_B, respectively.

Statistical Analyses. Statistical analyses were performed using Prism (GraphPad Software). Student's *t* test was used for comparisons between two groups. One-way ANOVA combined with the Tukey's post hoc test (63) was used for multiple comparisons. *F*-tests were performed to find differences in the stimulus frequency-dependence of NLC. In all statistical analyses, $P < 0.05$ was considered significant.

Data, Materials, and Software Availability. All study data are included in the article and/or *SI Appendix*.

ACKNOWLEDGMENTS. This work was supported by an NIH grant DC017482 (to K.H.) and by the Hugh Knowles Center. Some of the imaging work was performed at the Northwestern University Center for Advanced Microscopy generously supported by National Cancer Institute Cancer Center Support Grant P30 CA060553 awarded to the Robert H Lurie Comprehensive Cancer Center.

Author affiliations: [a]Department of Otolaryngology–Head and Neck Surgery, Feinberg School of Medicine, Northwestern University, Chicago, IL 60611; [b]Department of Communication Sciences and Disorders, Northwestern University, Evanston, IL 60208; and [c]The Hugh Knowles Center for Clinical and Basic Science in Hearing and Its Disorders, Northwestern University, Evanston, IL 60208

1. J. Zheng *et al.*, Prestin is the motor protein of cochlear outer hair cells. *Nature* **405**, 149–155 (2000).
2. S. L. Alper, A. K. Sharma, The SLC26 gene family of anion transporters and channels. *Mol. Aspects Med.* **34**, 494–515 (2013).
3. W. E. Brownell, C. R. Bader, D. Bertrand, Y. de Ribaupierre, Evoked mechanical responses of isolated cochlear outer hair cells. *Science* **227**, 194–196 (1985).
4. M. C. Liberman *et al.*, Prestin is required for electromotility of the outer hair cell and for the cochlear amplifier. *Nature* **419**, 300–304 (2002).
5. X. Wu, J. Gao, Y. Guo, J. Zuo, Hearing threshold elevation precedes hair-cell loss in prestin knockout mice. *Brain Res. Mol. Brain Res.* **126**, 30–37 (2004).
6. M. A. Cheatham, K. H. Huynh, J. Gao, J. Zuo, P. Dallos, Cochlear function in Prestin knockout mice. *J. Physiol.* **560**, 821–830 (2004).
7. M. A. Cheatham *et al.*, Evaluation of an independent prestin mouse model derived from the 129S1 strain. *Audiol. Neurootol.* **12**, 378–390 (2007).
8. P. Dallos *et al.*, Prestin-based outer hair cell motility is necessary for mammalian cochlear amplification. *Neuron* **58**, 333–339 (2008).
9. P. Dallos, B. N. Evans, High-frequency motility of outer hair cells and the cochlear amplifier. *Science* **267**, 2006–2009 (1995).
10. G. Frank, W. Hemmert, A. W. Gummer, Limiting dynamics of high-frequency electromechanical transduction of outer hair cells. *Proc. Natl. Acad. Sci. U.S.A.* **96**, 4420–4425 (1999).
11. J. E. Gale, J. F. Ashmore, An intrinsic frequency limit to the cochlear amplifier. *Nature* **389**, 63–66 (1997).
12. K. Grosh, J. Zheng, Y. Zou, E. de Boer, A. L. Nuttall, High-frequency electromotile responses in the cochlea. *J. Acoust. Soc. Am.* **115**, 2178–2184 (2004).
13. T. Ren, W. He, P. G. Barr-Gillespie, Reverse transduction measured in the living cochlea by low-coherence heterodyne interferometry. *Nat. Commun.* **7**, 10282 (2016).
14. J. Santos-Sacchi, W. Tan, The frequency response of outer hair cell voltage-dependent motility is limited by kinetics of prestin. *J. Neurosci.* **38**, 5495–5506 (2018).
15. J. Santos-Sacchi, W. Tan, Voltage does not drive prestin (SLC26a5) electro-mechanical activity at high frequencies where cochlear amplification is best. *iScience* **22**, 392–399 (2019).
16. A. Vavakou, N. P. Cooper, M. van der Heijden, The frequency limit of outer hair cell motility measured in vivo. *Elife* **8**, e47667 (2019).
17. J. B. Dewey, A. Altoe, C. A. Shera, B. E. Applegate, J. S. Oghalai, Cochlear outer hair cell electromotility enhances organ of Corti motion on a cycle-by-cycle basis at high frequencies in vivo. *Proc. Natl. Acad. Sci. U.S.A.* **118**, e2025206118 (2021).
18. R. D. Rabbitt, The cochlear outer hair cell speed paradox. *Proc. Natl. Acad. Sci. U.S.A.* **117**, 21880–21888 (2020).
19. P. Mistrík, N. Daudet, K. Morandell, J. F. Ashmore, Mammalian prestin is a weak Cl(-)/HCO(3)(-) electrogenic antiporter. *J. Physiol.* **590**, 5597–5610 (2012).

20. H. Mutai *et al.*, Diverse spectrum of rare deafness genes underlies early-childhood hearing loss in Japanese patients: A cross-sectional, multi-center next-generation sequencing study. *Orphanet J. Rare Dis.* **8**, 172 (2013).
21. S. Takahashi, M. A. Cheatham, J. Zheng, K. Homma, The R130S mutation significantly affects the function of prestin, the outer hair cell motor protein. *J. Mol. Med. (Berl).* **94**, 1053–1062 (2016).
22. Q. Liu *et al.*, Asymmetric pendrin homodimer reveals its molecular mechanism as anion exchanger. bioRxiv [Preprint] (2022), https://doi.org/10.1101/2022.01.14.476289 (Accessed 25 July 2022).
23. J. Ge *et al.*, Molecular mechanism of prestin electromotive signal amplification. *Cell* **184**, 4669–4679.e13 (2021).
24. N. Bavi *et al.*, The conformational cycle of prestin underlies outer-hair cell electromotility. *Nature* **600**, 553–558 (2021).
25. C. Butan *et al.*, Single particle cryo-EM structure of the outer hair cell motor protein prestin. *Nat. Commun.* **13**, 290 (2022).
26. H. Futamata *et al.*, Cryo-EM structures of thermostabilized prestin provide mechanistic insights underlying outer hair cell electromotility. *Nat. Commun.* **13**, 6208 (2022).
27. J. D. Walter, M. Sawicka, R. Dutzler, Cryo-EM structures and functional characterization of murine Slc26a9 reveal mechanism of uncoupled chloride transport. *Elife* **8**, e46986 (2019).
28. X. Chi *et al.*, Structural insights into the gating mechanism of human SLC26A9 mediated by its C-terminal sequence. *Cell Discov.* **6**, 55 (2020).
29. D. Oliver *et al.*, Intracellular anions as the voltage sensor of prestin, the outer hair cell motor protein. *Science* **292**, 2340–2343 (2001).
30. J. Santos-Sacchi, L. Song, Chloride anions regulate kinetics but not voltage-sensor Qmax of the solute carrier SLC26a5. *Biophys. J.* **110**, 2551–2561 (2016).
31. J. Santos-Sacchi, L. Song, J. Zheng, A. L. Nuttall, Control of mammalian cochlear amplification by chloride anions. *J. Neurosci.* **26**, 3992–3998 (2006).
32. D. Gorbunov, J. Hartmann, V. Renigunta, D. Oliver, "A glutamate scan identifies an electrostatic switch for prestin activity" in *41st Annual MidWinter Meeting of the Association for Research in Otolaryngology* (Association for Research in Otolaryngology, San Diego, CA, 2018), pp. 626–627.
33. D. Oliver, D. Gorbunov, J. Hartmann, D. Lenz, V. Renigunta, An electrostatic switch for gating the electromechanical activity of SLC26A5 (prestin). *Biophys. J.* **116**, 169a (2019).
34. T. Yamashita *et al.*, Normal hearing sensitivity at low-to-middle frequencies with 34% prestin-charge density. *PLoS One* **7**, e45453 (2012).
35. K. Homma, S. Takahashi, M. A. Cheatham, How much prestin motor activity is required for normal hearing? *Hear Res.* **423**, 108376 (2022), 10.1016/j.heares.2021.108376.
36. D. I. Scheffer, J. Shen, D. P. Corey, Z. Y. Chen, Gene expression by mouse inner ear hair cells during development. *J. Neurosci.* **35**, 6366–6380 (2015).
37. H. Liu *et al.*, Cell-specific transcriptome analysis shows that adult pillar and deiters' cells express genes encoding machinery for specializations of cochlear hair cells. *Front Mol. Neurosci.* **11**, 356 (2018).
38. J. Orvis *et al.*, gEAR: Gene expression analysis resource portal for community-driven, multi-omic data exploration. *Nat. Methods* **18**, 843–844 (2021).
39. T. J. Schaechinger, D. Oliver, Nonmammalian orthologs of prestin (SLC26A5) are electrogenic divalent/chloride anion exchangers. *Proc. Natl. Acad. Sci. U.S.A.* **104**, 7693–7698 (2007).
40. K. Wasano *et al.*, Systematic quantification of the anion transport function of pendrin (SLC26A4) and its disease-associated variants. *Hum. Mutat.* **41**, 316–331 (2020).
41. M. R. Dorwart, N. Shcheynikov, Y. Wang, S. Stippec, S. Muallem, SLC26A9 is a Cl(-) channel regulated by the WNK kinases. *J. Physiol.* **584**, 333–345 (2007).
42. M. H. Chang *et al.*, Slc26a9–anion exchanger, channel and Na+ transporter. *J. Membr. Biol.* **228**, 125–140 (2009).
43. S. L. Johnson, M. Beurg, W. Marcotti, R. Fettiplace, Prestin-driven cochlear amplification is not limited by the outer hair cell membrane time constant. *Neuron* **70**, 1143–1154 (2011).
44. J. Li *et al.*, PIEZO2 mediates ultrasonic hearing via cochlear outer hair cells in mice. *Proc. Natl. Acad. Sci. U.S.A.* **118**, e2101207118 (2021).
45. J. Li *et al.*, Prestin-mediated frequency selectivity does not cover ultrahigh frequencies in mice. *Neurosci. Bull.* **38**, 769–784 (2022).
46. X. Z. Liu *et al.*, Prestin, a cochlear motor protein, is defective in non-syndromic hearing loss. *Hum. Mol. Genet.* **12**, 1155–1162 (2003).
47. D. Navaratnam, J. P. Bai, H. Samaranayake, J. Santos-Sacchi, N-terminal-mediated homomultimerization of prestin, the outer hair cell motor protein. *Biophys. J.* **89**, 3345–3352 (2005).
48. J. Santos-Sacchi, S. Kakehata, T. Kikuchi, Y. Katori, T. Takasaka, Density of motility-related charge in the outer hair cell of the guinea pig is inversely related to best frequency. *Neurosci. Lett.* **256**, 155–158 (1998).
49. C. Corbitt, F. Farinelli, W. E. Brownell, B. Farrell, Tonotopic relationships reveal the charge density varies along the lateral wall of outer hair cells. *Biophys. J.* **102**, 2715–2724 (2012).
50. S. Mahendrasingam, M. Beurg, R. Fettiplace, C. M. Hackney, The ultrastructural distribution of prestin in outer hair cells: A post-embedding immunogold investigation of low-frequency and high-frequency regions of the rat cochlea. *Eur. J. Neurosci.* **31**, 1595–1605 (2010).
51. D. Z. He, P. Dallos, Somatic stiffness of cochlear outer hair cells is voltage-dependent. *Proc. Natl. Acad. Sci. U.S.A.* **96**, 8223–8228 (1999).
52. D. Z. He, S. Jia, P. Dallos, Prestin and the dynamic stiffness of cochlear outer hair cells. *J. Neurosci.* **23**, 9089–9096 (2003).
53. M. A. Cheatham *et al.*, Loss of the tectorial membrane protein CEACAM16 enhances spontaneous, stimulus-frequency, and transiently evoked otoacoustic emissions. *J. Neurosci.* **34**, 10325–10338 (2014).
54. P. Hofstetter, D. Ding, N. Powers, R. J. Salvi, Quantitative relationship of carboplatin dose to magnitude of inner and outer hair cell loss and the reduction in distortion product otoacoustic emission amplitude in chinchillas. *Hear Res.* **112**, 199–215 (1997).
55. K. Homma, C. Duan, J. Zheng, M. A. Cheatham, P. Dallos, The V499G/Y501H mutation impairs fast motor kinetics of prestin and has significance for defining functional independence of individual prestin subunits. *J. Biol. Chem.* **288**, 2452–2463 (2013).
56. J. Santos-Sacchi, S. Kakehata, S. Takahashi, Effects of membrane potential on the voltage dependence of motility-related charge in outer hair cells of the guinea-pig. *J. Physiol.* **510**, 225–235 (1998).
57. K. Homma, P. Dallos, Evidence that prestin has at least two voltage-dependent steps. *J. Biol. Chem.* **286**, 2297–2307 (2011).
58. L. D. Liberman, J. Suzuki, M. C. Liberman, Dynamics of cochlear synaptopathy after acoustic overexposure. *J. Assoc. Res. Otolaryngol.* **16**, 205–219 (2015).
59. J. Zheng *et al.*, The C-terminus of prestin influences nonlinear capacitance and plasma membrane targeting. *J. Cell Sci.* **118**, 2987–2996 (2005).
60. S. Takahashi *et al.*, Susceptibility of outer hair cells to cholesterol chelator 2-hydroxypropyl-beta-cyclodextrine is prestin-dependent. *Sci. Rep.* **6**, 21973 (2016).
61. M. Müller, K. von Hünerbein, S. Hoidis, J. W. Smolders, A physiological place-frequency map of the cochlea in the CBA/J mouse. *Hear Res.* **202**, 63–73 (2005).
62. W. S. Cleveland, Robust locally weighted regression and smoothing scatterplots. *J. Am. Stat. Assoc.* **74**, 829–836 (1979).
63. J. W. Tukey, *Exploratory Data Analysis* (Wesley Publishing Company, Reading, MA, 1977).